# LANGMUIR

pubs.acs.org/Langmuir Article

### Cell Membrane Oscillations under Radiofrequency Electromagnetic Modulation

Li Lin,\* Marshall R. McCraw, Berkin Uluutku, Yi Liu, Dayun Yan, Vikas Soni, Alex Horkowitz, Xiaoliang Yao, Ruby Limanowski, Santiago D. Solares, Isak I. Beilis, and Michael Keidar\*



Cite This: Langmuir 2023, 39, 3320-3331

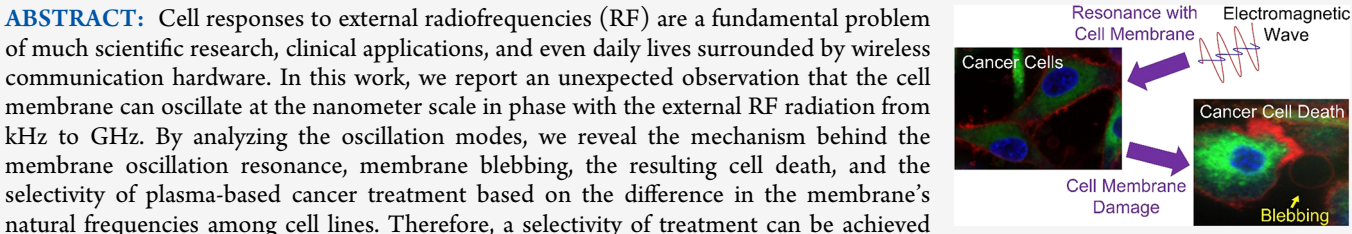


**ACCESS** I

III Metrics & More

ABSTRACT: Cell responses to external radiofrequencies (RF) are a fundamental problem of much scientific research, clinical applications, and even daily lives surrounded by wireless communication hardware. In this work, we report an unexpected observation that the cell membrane can oscillate at the nanometer scale in phase with the external RF radiation from kHz to GHz. By analyzing the oscillation modes, we reveal the mechanism behind the membrane oscillation resonance, membrane blebbing, the resulting cell death, and the selectivity of plasma-based cancer treatment based on the difference in the membrane's

by aiming at the natural frequency of the target cell line to focus the membrane damage on



Article Recommendations

the cancer cells and avoid normal tissues nearby. This gives a promising cancer therapy that is especially effective in the mixing lesion of the cancer cells and normal cells such as glioblastoma where surgical removal is not applicable. Along with these new phenomena, this work provides a general understanding of the cell coupling with RF radiation from the externally stimulated membrane behavior to the cell apoptosis and necrosis.

#### INTRODUCTION

Radiofrequency (RF) electromagnetic (EM) waves' interactions with living cells have been considered extensively over a few decades. 1-3 The importance of this kind of interaction stems from the fact that living organisms on Earth are not adapted well to RF radiation because, under natural conditions, some of the wavelengths are practically absent due to strong absorption by the rotational mode of water molecules on Earth's atmosphere. 4 To this end, several important discoveries were reported, such as the dependence of the RF-cell interactions on frequency when various microorganisms are irradiated.<sup>5-8</sup> In addition, in vivo studies were performed to evaluate the effect of RF on tumors and the growth of cells damaged by ionizing radiation. The power was applied via acupuncture points. These experiments showed that RF at nonthermal intensities normalizes the growth of cells damaged by ionizing radiation. Moreover, their action on biologically active zones in animals has an immunomodulation effect. Overall, an intense program dedicated to studying RF with biological organisms led to the conclusion that such interactions do not depend on the intensity of EM waves and have a resonance nature. In addition, it has been established that biological objects "remember" the effect of EM radiation for a relatively long time (slow deactivation). This is in line with the activation effect observed during cold atmospheric plasma treatment.<sup>10</sup> Deformation and electroporation of the cell membrane were associated with the action of an external electric field. <sup>11</sup> An AC electric field can lead to a nonlinear cell response, and even a modest externally applied field could generate a very large local field within the membrane. In contrast, the spherical symmetry relevant to suspensions of spherical cells was considered where proteins catalyze a reaction. 12 The AC field can cause the enzyme to pump ions or molecules through the membrane against an electrochemical potential. The efficiency of this energy transduction can be as high as 25%. 12 In another study, it was demonstrated that an electric field applied wirelessly can regulate intracellular signaling and cell function in a frequencydependent manner.<sup>13</sup> As a result, electric field distribution in the cell is strongly nonuniform and sensitive to the cell's physical properties and environment. According to the vast literature, it is known that the permeability and uptake of cells can be enhanced by the electric field.<sup>14</sup> Many studies focused on EM field generation within cells and its role in regulating biological processes. To that end, Frolich suggested that biological cells may exhibit high-frequency electrical oscillations (GHz to THz) with the source of oscillations emanating from the cell membrane due to its high transmembrane potential. This is also confirmed by a recent

Received: November 23, 2022 Revised: January 25, 2023 Published: February 20, 2023





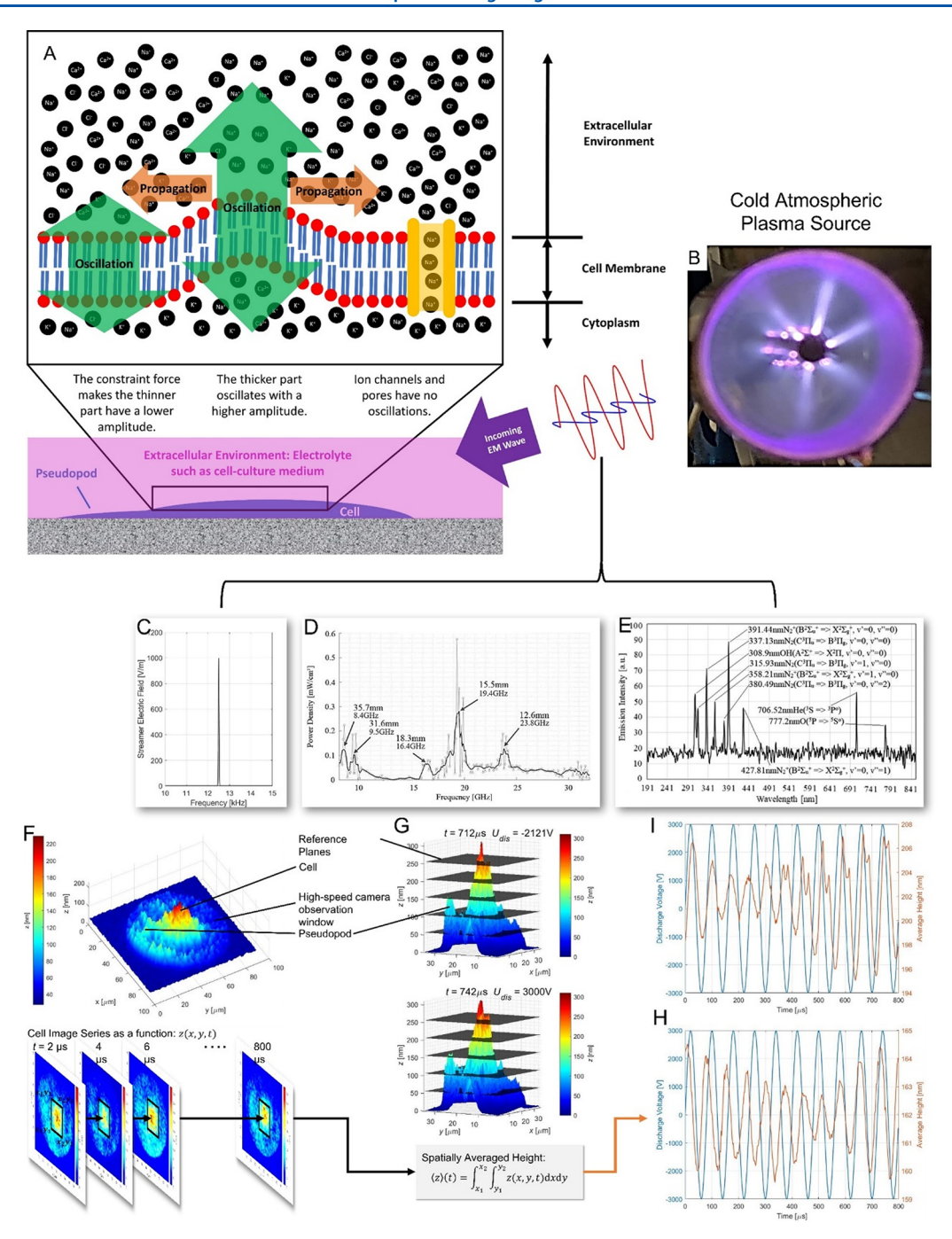


Figure 1. Example of spatially and temporally resolved real-time observation of cell membrane oscillation. (A) Ions surrounding a cell oscillate due to coupling with the external electromagnetic field. Some ions can pass through the cell membrane while others collide on the membrane leading to membrane oscillation. (B) Discharge tube containing He-air cold atmospheric plasma is used as a multiple-frequency radiation source to oscillate the cell membrane. The power spectrum includes the following: (C) discharge frequency with a small bandwidth; (D) plasma frequency at GHz, reproduced with permission; and (E) UV-VIS optical emissions, reproduced with permissions. (F) 3D cell image of an A549 cell line. (G) Height increments along with the discharge voltage over time. (H) Temporally resolved and spatially averaged cell height versus the external electric field waveform as the discharge voltage of the discharge tube. (I) Another example of A549 cell line height versus the external electric field waveform of the plate electrodes. from ref 27, copyright 2019, AIP Publishing

numerical simulation work reflecting the membrane oscillation under microwave exposure.<sup>17</sup> When an electromagnetic wave is an incident on a cell, sound waves across and along the interface (membrane) are produced.<sup>18,19</sup> The viscoelastic properties of the membrane control such waves, and under some relevant conditions, resonance behavior might be expected. As reported by multiple researchers, the cell membrane's electric potential is built due to the membrane

surface charges and an ion cloud surrounding the cell.<sup>20,21</sup> The external AC EM field thus oscillates the ions bound to the membrane and should lead to membrane oscillations and cell deformations. Therefore, the cell membrane oscillation could be observed in phase with the external excitation, and the membrane should be able to respond to lower frequencies, such as the kHz, which are not yet studied.

On the other hand, a newly developed research field, plasmabased cancer therapy, is becoming a promising and attractive treatment for solid and diffuse tumors, particularly brain tumors.<sup>22</sup> Cold atmospheric plasmas (CAPs) are usually used in plasma therapy. The most significant advantage of such an approach is the selectivity, which can kill more cancerous cells causing limited damage to normal cells. 23,24 In the last decade, many papers have reported that plasma therapy relies on plasma chemistry, such as the reactive oxygen and nitrogen species (RONS). These species are generated in the streamer discharge in the open air, triggering oxidative stress, cell cycle arrest, and DNA damage and finally leading to apoptosis.<sup>23,24</sup> However, according to recent reports, the RF emissions from cold plasma can also lead to a combination of apoptosis and necrosis.<sup>25</sup> Therefore, investigating the cell responses to external RF radiation, especially the VLF waves and microwaves, becomes urgent.

This paper reports RF electromagnetic field coupling with the cellular membrane and cell membrane oscillation under external electromagnetic field excitation. The nm-scale oscillations are observed in real time using a laser Michelson interferometer with mode analysis. We also observed that the oscillations at kHz can lead to cavitations and finally kill the cells. We also found the natural frequencies of multiple cell lines and explained the selectivity of RF treatment on cells based on resonance. A physical mechanism behind the plasma treatment is thus proposed. When a strong cell membrane oscillation is raised due to the resonance and thus membrane damage, cavitations may also occur in the vicinity of the cell and lead to bubbling.

#### RESULTS AND DISCUSSION

As mentioned in the introduction, cell membrane oscillation could occur as a result of ion oscillations that can affect the membrane. However, there are pores and ion channels on the membrane through which charges can move freely when these gates open. The number of ion channels and pores on the cell membrane also varies among cell types. Application of an electric field can lead to the electroporation opening and stimulating voltage-gated Na, Ca, and K channels. Also, an oscillation component at a certain location on the cell membrane can propagate as a transverse wave along the membrane. This means that an external electric field can also open mechanosensitive channels. Considering the mechanism of the cell membrane oscillations and their transverse waves, one should consider that the interior structures such as proteins and DNA are negatively charged. On the other hand, the cytoplasm is K<sup>+</sup>-rich, and the extracellular vicinity usually includes more Ca2+, Na+, and Cl-20 As the interior K+ attaches to the negatively charged inner phospholipid heads, 20 an external EM wave can "shake" these ions and oscillate the membrane (Figure 1A). The positive ions surrounding the cell can cause oscillation of the membrane as well. However, the extracellular medium (several Debye lengths away from the membrane) is quasi-neutral and gives no significant response to the external EM wave. This implies that an open ion channel or pore should be immune to the ion impacts because it lets the ions go through. Therefore, the charges that pass through the membrane apply no force to the membrane.

We employed a laser Michelson interferometer coupled with a high-speed camera for 3D single-cell imaging to observe the oscillation. The camera is synchronized with the external RF radiation source. Details of the setup are introduced in the Materials and Methods section at the end of this article. This work uses two external RF sources: a pair of electrodes powered by a single 6000 V AC at 12.5 kHz VLF and a discharge tube containing a helium-air CAP (Figure 1B) as a multiple-frequency source. The CAP emission includes three major wavelength groups (Figure 1A). First, the discharge tube generator exhibits a radial streamer propagation. This means that the streamer discharge repeats at the power supply frequency of 12.5 kHz with a small bandwidth, which will be discussed later (Figure 1C). Second, the electron oscillations in a CAP provide multiple microwave emissions at GHz, which has been reported in previous works (Figure 1D). 25,26 Third, there are photon emissions from the excited species, mainly in the UV–VIS range (Figure 1E). 29

The resulting cell oscillation data can be analyzed as a square matrix: the spatial distribution of heights. Cell oscillation over time is thus a movie containing a series of these images over time. The 3D height data z is a function of both 2D space and time. In this work, such a set of data is considered as a matrix z(x, y, t). Obviously, z(x, y, t) is a movie of cell oscillation, and a gif example can be found at https://mpnl.seas.gwu.edu/ open-codes/. A snapshot of an A549 line cell under the discharge tube radiation is shown where the cell is a 300 nm object higher than the Petri dish bottom located at the center of the round observation window (Figure 1F). A pseudopod as an extended structure with about 150 nm height can be found on the left of the cell. The thickest part of the cell with the largest volume is easier to oscillate and has the largest amplitude, while the thinner part at the edge suffers more constraint from the dish bottom. Figure 1G shows two sideview examples of it and several height reference planes to demonstrate the cell height oscillations under the external EM field. At about 712  $\mu$ s, the discharge voltage is about -2000 V. The pseudopod is lower than the 160 nm reference plane, and the cell center has only one peak higher than the 260 nm reference plane. When the time is 742  $\mu$ s, the discharge voltage is at 3000 V; one can observe the highest positions of the membrane of both the pseudopod and the cell center. Numerically integrating the height data of the pixels around the cell center yields the spatially averaged height as a function of time only where  $\langle z(t) \rangle = \int_{x_1}^{x_2} \int_{y_1}^{y_2} z(x, y, t) dxdy$ . The temporally resolved height is thus shown in Figure 1H along with the external EF waveform. The waveforms are in-phase, indicating the causality between them. The waveforms shown in Figure 1I are another A549 cell exposure in the EF of the pair of plate electrodes.

Due to the complex structure of a cell, including the organelles, cytosol, cytoskeleton, etc., cell oscillation is a superposition of multiple oscillation modes. These modes are acquired by applying proper orthogonal decomposition (POD) on the cell oscillation movie z(x, y, t). As a variation of singular value decomposition (SVD), POD makes<sup>30,31</sup>

$$\mathbf{z}_{XY\times\tau}(x, y, t) = \mathbf{U}_{XY\times M}(x, y, m)\mathbf{S}_{M\times M}(m)\mathbf{V}_{\tau\times M}^{T}(m, t)$$
(1)

where the subscripts X, Y,  $\tau$ , and M represent the total x pixel number, the total y pixel number, the frame number, and the total mode number, respectively. The superscript T represents the transpose of a matrix. In eq 1, the matrix z is in the form of stacking all the rows of a 2D image in a single column, in other words, making a 2D image into a 1D array, while the column can represent the time. Therefore, the matrix z in POD is XY

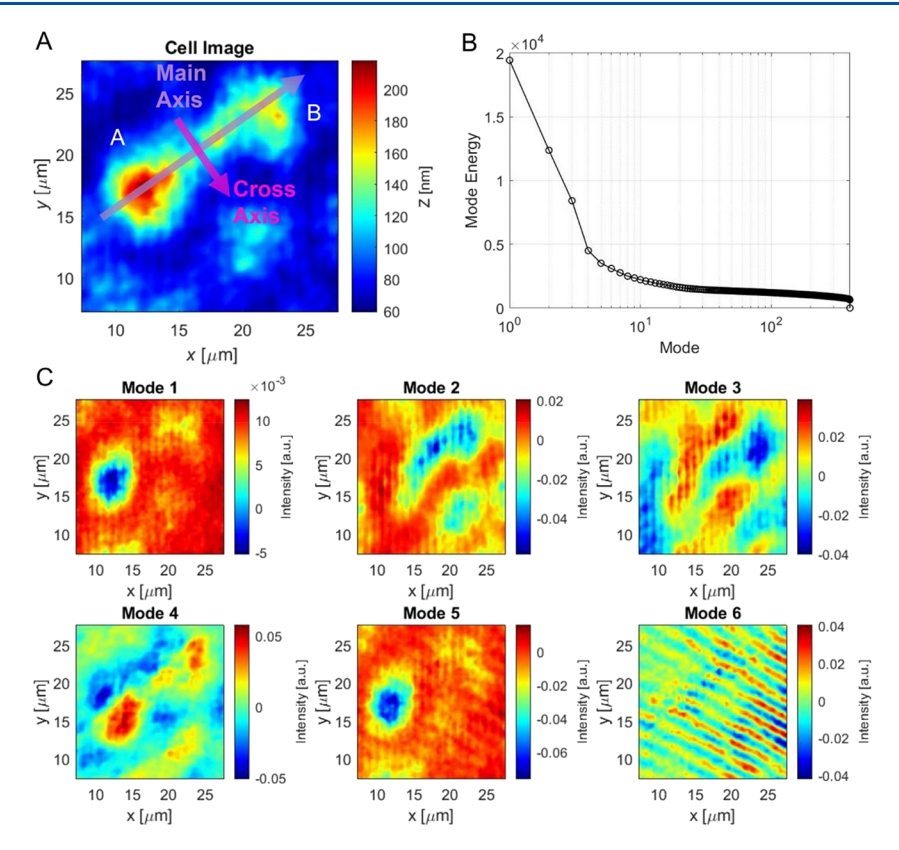


**Figure 2.** Cell image, S matrix, and first 6 modes of the U87MG example after using the proper orthogonal decomposition on the cell oscillation movie. (A) Cell image of this example where a U87MG cell is dividing into two daughter cells is marked as A and B. (B) S matrix is a diagonal matrix where the diagonal contains the energy of each mode. Only the first couple of modes have the most energy: the contribution to the oscillation. (C) U matrix contains the modes of oscillation, and the first 6 of them are plotted.

rows by  $\tau$  columns, but it is still a height function of space and time. The matrix U shows the appearance of each mode with m as the index of the mode number. The diagonal matrix S is M by M, and its diagonal is a list of energy of each mode. The energy values are the singular values, in other words, the contributions of oscillation amplitudes of modes. It is also common to consider that the energy values are the eigenvalues of an oscillation while the modes are eigenvectors. The matrix V is  $\tau$  by M, representing the oscillation of each mode over time.

An example of a U87MG cell line is shown in Figures 2 and 3. Figure 2A is the cell image, and, interestingly, the cell is dividing. Therefore, to help us study the modes later, we can define the main axis through the two daughter cells (perpendicular to the equatorial plane) and a cross-axis along the equatorial plane. Figure 2B is the list of singular values. The descending sorting is contained in the POD and SVD, defining the mode with the highest contribution to the oscillation as the first mode. A list of the first 6 modes is shown in Figure 2C. Mode 1 shows a negative height change for daughter cell A on the left and a positive one for daughter cell B on the right. This is thus an eigenvector, or in other words, an oscillation component along the main axis. Modes 2, 3, and 4 are the oscillation components along the cross-axis but with different meanings. Mode 4 allows the two daughter cells to oscillate in phase, but their left and right parts are negative and positive, respectively. Mode 2 allows daughter cell A to have the left part to be positive and the right part negative while daughter cell B makes them negative entirely. Mode 3 allows the daughter cell B to have left positive and right negative while

leavening the daughter cell A positive. Mode 6 shows stripes over the entire observation region. These are transverse waves of the liquid medium due to the cell membrane oscillations, while Mode 5 shows their coupling. The wavelength in the liquid is about 2.5  $\mu$ m. Because no two cells look the same, the mode images of the experimental repeats, even for the same cell line under the same experimental condition, look different. Therefore, Figure 2 is merely an example to show the concept of mode analysis using POD. The comparison among cell lines with statistical studies will be discussed in the next section, where different features of different cells can be found.

The oscillation modes are used to analyze the resonance between the cell membrane and the external EM waves. In this section, we will consider such a resonance condition. The wave equation of an arbitrary 2D viscoelastic membrane that has been derived in previous works can be used<sup>32,33</sup>

$$D\nabla^4 z + \rho_m \frac{\partial^2 z}{\partial t^2} = 0 \tag{2a}$$

$$D = \frac{Q_m(f)d_{th}^2}{12(1 - v^2)} \tag{2b}$$

where  $\rho_m$  is the mass density of the membrane, which is about  $1.02~{\rm g/m^3}$ ,  $Q_m$  is the frequency-dependent viscoelastic modulus of the membrane in the Fourier domain,  $d_{th}$  is the thickness of the cell membrane assumed at 10 nm, and  $\nu$  is the Poisson ratio of the cell at around 0.49 in average. The viscoelastic modulus of each cell line is obtained directly through spectral inversion of AFM FD curves and is shown in Figure 3A. These values are all at around several kPa, which agrees

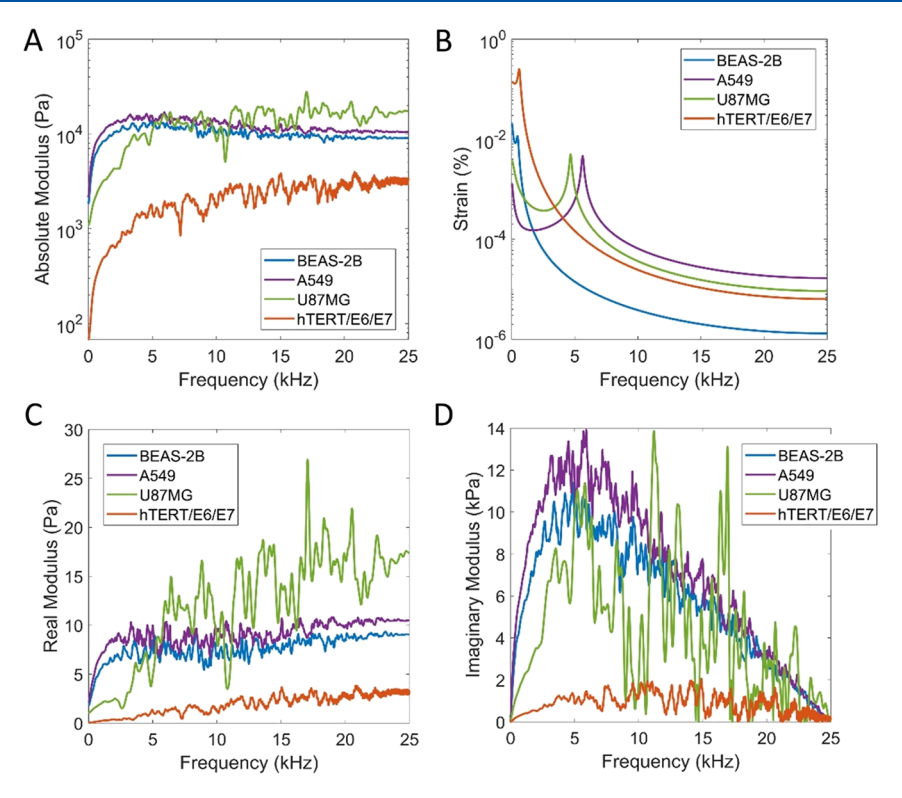


Figure 3. Mechanical properties of cell membranes are measured using atomic force microscopy. (A) Absolute modulus of the cell lines: A549, BEAS-2B, U87MG, and hTERT/E6/E7. The cell responses approach their equilibrium moduli of around 10 kPa when the frequency passes 6 kHz. (B) Simulated strain response of each cell line oscillating at their primary natural frequency under equal harmonic stresses, demonstrating that hTERT/E6/E7 oscillates with the largest magnitude and A549, the least. (C) Real and (D) imaginary parts of the experimentally obtained relaxance. The real part of the relaxance is attributed to the elastic behavior of the materials while the imaginary part is attributed to dissipative behavior.

well with other prior publications.<sup>39–42</sup> Considering  $z(r, t) = z_0(r) \exp(i2\pi ft)$  as the spatially and temporally resolved oscillation amplitude, the wave equation can be reduced to<sup>32</sup>

$$\nabla^2 \mathbf{z}_0 + \Lambda^2 \mathbf{z}_0 = 0 \tag{3}$$

where  $\Lambda$  is a function of the resonant frequency. Combining eq 3 with the oscillation of each mode, one can have

$$\nabla^2 \mathbf{z}_{0\eta} + \Lambda_{\eta}^2 \mathbf{z}_{0\eta} = 0 \tag{4}$$

where the subscript  $\eta$  represents the  $\eta$ th oscillation modes. Thus, the resonant frequencies of modes are

$$f_{\eta} = \frac{\Lambda_{\eta}^2}{2\pi} \sqrt{\frac{D}{\rho_m}} \tag{5}$$

The parameters  $\Lambda_{\eta}^{\ 2}$  can be calculated using the POD results. Taking the modes of the U87MG example into eq 5, natural frequency distributions for each mode can be found as shown in Figure 4. As the most significant mode, Mode 1 shows a clear ring of high natural frequencies distributed at the cell boundary of the daughter cell A with values around 10 kHz. On a ring-like distribution, some regions have a frequency up to 15 kHz, while most of the ring has a frequency much lower. The periphery of the membrane always has a higher natural frequency than other regions in the images. This can also be found in Modes 2 and 3 in Figure 4, but with a lower value. Figure 4 also shows that the cell's main body has a natural frequency of around 3 kHz. However, considering that the most contribution to the oscillation is from Mode 1, one can

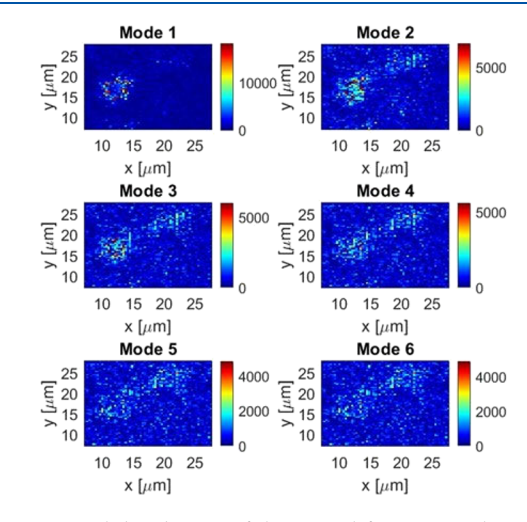


Figure 4. Spatial distribution of the natural frequency values (shown by colors in Hz) of the first 6 modes of the U87MG example.

consider that the cell membrane with a natural frequency of 10 to 15 kHz plays the most important role.

In Figure 5, the average membrane natural frequencies of the 6 cell lines and their first 9 modes are compared. The cell lines contain 3 normal-cancer pairs: hTERT/E6/E7 (normal astrocyte) versus U87MG (malignant gliomas), L929 (normal fibroblast) versus B16F10 (melanoma), and BEAS-2B (normal lung tissue cell) versus A549 (lung carcinoma epithelial cell). For all cell lines, Mode 1 always has the highest natural frequency. The expected strain response of each cell at their

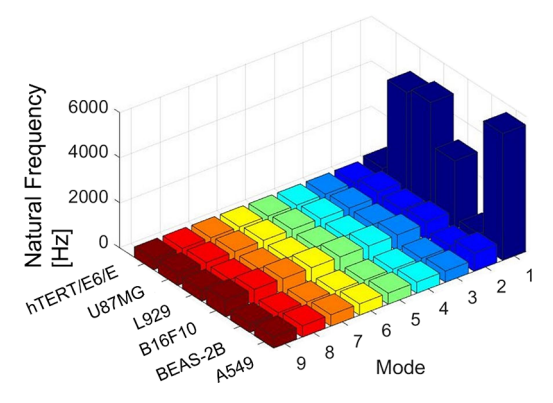


Figure 5. Natural frequencies are spatially averaged at the membrane area and compared among cell lines.

primary natural frequency can then be calculated using a standard linear solid (SLS) model fit to the viscoelastic modulus obtained from the AFM, as seen in eq 6. The values of these

$$\varepsilon_{f\eta}(z) = \frac{1}{Q(z)} \left[ \frac{z \sin(2\pi f_{\eta} \Delta t)}{z^2 - 2z \cos(2\pi f_{\eta} \Delta t) + 1} \right]$$
(6)

strain responses are shown in Figure 3B, demonstrating that hTERT/E6/E7 oscillates the most while A549 oscillates the least. The frequency of U87MG is higher than the value of hTERT/E6/E7, which means that Mode 1 (the most contribution mode) of U87MG has a closer frequency to the plasma treatment discharge frequency at 12.5 kHz. This may explain the selectivity where more U87MG cells can be killed than the hTERT/E6/E7 by the electromagnetic emissions from the plasma where the discharge frequency has a bandwidth due to the particle thermal velocities. 43 In another previous work, one can find a higher sensitivity of hTERT/E6/ E7 to chemical treatment, causing more apoptosis of it compared with U78MG. At the same time, the fact that only the physical emissions from the plasma can kill more hTERT/ E6/E7 is confirmed.<sup>44</sup> Similarly, we can also explain the selectivity for the pair of A549 and BEAS-2B. Interestingly, the Mode 1 natural frequency of B16F10 is lower than L929. This suggests that B16F10 should be harder to kill through the treatment than L929 as it exhibits a reversed selectivity. Figure 5 implies that B16F10 is harder to be killed than the other two cancer cell lines. This agrees with a previous observation.<sup>46</sup> Please note that the term "kill" above contains both apoptosis and necrosis, which will be discussed in the next paragraph. Overall, we can conclude that the natural frequency comparison among these cell lines at the current stage agrees with the selectivity relations of plasma treatment results reported previously. However, one can pose a question: why do large resonant oscillations on the membrane kill cells? As shown in Figure 3B, the expected strain under resonance oscillation can be amplified more than 100 times. This will be answered in the following discussions. The relaxance shown in Figure 3C,D will be discussed in the Materials and Methods

When the modulus is sub-MPa, as some other publications introduced, <sup>36,47</sup> the resulting resonant frequencies are usually at several kHz. Note that the modulus of a cell as a whole varies from kPa to MPa depending on the cell status: attached to a wall or floating, living or dead, etc. <sup>40</sup> The resonance thus

makes extreme cell membrane oscillations at kHz and can thus lead to two probable phenomena. The first one is the cell membrane blebbing that localized decoupling of the cytoskeleton, causing the membrane bulge. These bulges can have a bubble-like appearance as shown in Figure 6. Figure

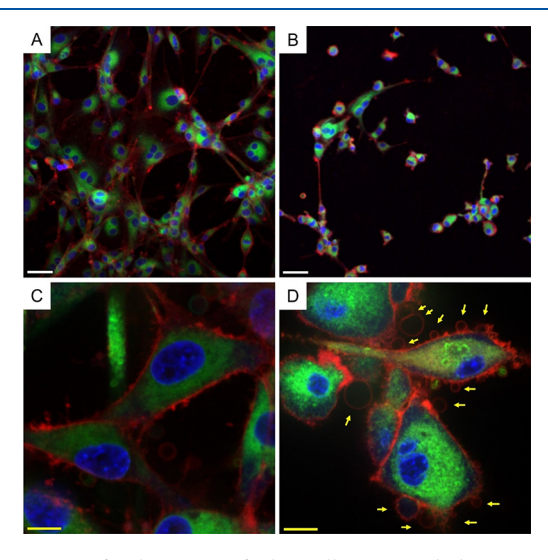


Figure 6. Confocal images of physically triggered damage on the U87MG cells membrane. (A) Control group before the plasma treatment. (B) Image of 10 min after a 60 s exposure to plasma radiation. (C) Zoomed-in image of the subplot (A). (D) Zoomed-in image of the subplot (B). Cell membrane, microtubules, and DNA (nucleus) were shown in red, green, and blue, respectively. Yellow arrows marked some obvious bubbles on the cell membranes. The images were taken using a Carl Zeiss 710 spectral confocal microscope. Scale bars were 50  $\mu$ m (white) and 10  $\mu$ m (yellow). The detailed protocols are listed in the Materials and Methods section.

6A,C shows the control group where the U87MG cells are cultured in the media without plasma treatment. Figure 6B,D shows the image taken 10 min after the U87MG cells were exposed to the discharge tube CAP for 30 s. As marked by yellow arrows, the fluorescence imaging revealed the formation of bubbles on the cell membrane, which might be due to the physical damage to the cell membrane and the following leakage of cellular solutions because the red staining of the microbubbles' membrane suggests that these membranes originated from cell membranes. The second probable result of the membrane oscillation is the cavitations next to the cell membranes. This phenomenon might be less probable compared with membrane blebbing. However, one should not exclude it when the membrane has a strong oscillation due to the resonance. Cavitation microbubbles may have the same appearance as shown in Figure 6. Considering that 10-15 kHz is in the range of ultrasound, the resonance thus leads to an interesting concept that an external EM wave can be an alternative source of sonodynamic therapy (SDT), and this work thus connects two research fields: the plasma medicine and SDT. According to the theory of SDT, ultrasound can oscillate the membrane mechanically and leads to cavitation in the vicinity.<sup>48</sup> The collapse of bubbles at cavitation centers results in a microenvironment containing a pulse temperature of 10<sup>4</sup> K with an about 80 MPa pressure variation. 49 Such a microenvironment thus becomes a chemical reactor that generates RONS. 50,51 RONS leading to cell apoptosis is wellknown and has been studied extensively for over a decade in

plasma medicine.<sup>23,52,53</sup> On the other hand, it is established that SDT leads to necrosis mechanically.<sup>54</sup> This explains the special kind of cell death reported previously in the plasma medicine community.<sup>24,25,55</sup> Of course, if it is true that plasma radiation can make cavitations, such an effect should be much more local and weaker than the one of SDT.

In Figure 7, the results of cell viability (U87MG cell line), which has been tested under 5 conditions, are shown. The

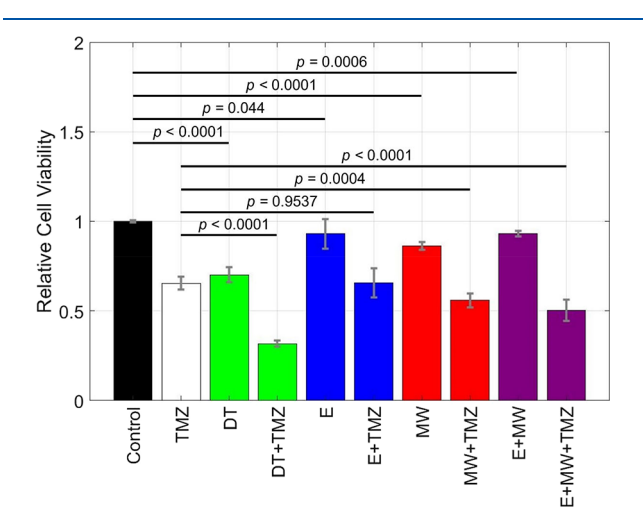


Figure 7. U87MG sensitization test. Control: the cells with no treatment. TMZ: the cells were treated with temozolomide. DT: the cells were treated with the discharge tube, which contains three main power spectrum bands. E: the cells were treated with a pair of plate electrodes, which are kept at 12.5 kHz. MW: the cells were treated with a microwave horn antenna, which has a frequency sweep from 8 to 18 GHz. The p values shown in the figure represent the statistical significance computed using Student's t test. For the detailed protocol, see the Materials and Methods section.

strongest response is achieved by using a 7 min treatment of a discharge tube. Combining with a brain cancer drug temozolomide (TMZ), one can reach more than 60% cell death. However, there is no such significant cell death under the treatment of the plate electrodes, although TMZ still works well. There is also statistically significant cell death when a sweep-frequency (8-18 GHz) microwave treatment is applied with and without TMZ and electrodes. However, these effects are weaker than those with the discharge tube, implying that the kHz VLF emissions (Figure 1C) from the discharge tube and the plate electrodes should be about to resonate with the cell membranes. In contrast, the GHz plasma oscillation frequencies can resonate with certain substructures of cells. For example, smaller nanovesicles can have membrane modulus values close to GPa, resulting in resonant frequencies over MHz and even close to GHz. 35,56 Microfilaments, microtubules, and DNA structures can have modulus over GPa<sup>42</sup> and thus have a natural frequency over GHz. Therefore, the external GHz frequency can also lead to cell death. Interestingly, the plate electrode treatment with the same 12.5 kHz as the discharge tube has very limited treatment effects. We excluded the reason for field amplitude. The amplitude of the electrode's EF is about  $2 \times 10^4 \text{ V/m}$ , and the resulting amplitude in the dish is about  $9 \times 10^4$  V/m, which is stronger than the plasma at around 1000 V/m (see Materials and Methods). Nevertheless, the electrodes have a much lower effect compared with the discharge tube. Therefore, it shows the superiority of plasma that the 12.5 kHz repetition rate has a

bandwidth as mentioned due to the randomness and uncertainty of particle motion during the streamer discharge. Such bandwidth can thus cover the natural frequencies of many cells while the electrodes can only aim at 12.5 kHz exactly.

#### CONCLUSIONS

In this work, we observed previously unknown nanometerscale cell membrane oscillation at kHz in-phase with the external electric field. The oscillations, considering the spatially and temporally resolved cell geometry, were analyzed using POD. The mode matrices show the oscillations of cells and the resulting liquid media waves with wavelengths visualized. The cell membrane oscillation under the external electric field results from strong charge oscillations near the membrane. The natural frequencies of the cell membranes were calculated using the POD mode analysis of the 2D viscoelastic membrane equation and the data acquired from the AFM. Due to the resonance of the cell membrane, these oscillations are enhanced and result in membrane damage and probably cavitation near the membrane. The former leads to cell necrosis and also blebbing while the latter leads to microbubbles in the media. The collapsing of microbubbles produces ROS to make cell apoptosis. Therefore, it can be concluded that cell lines with natural frequencies closer to the external RF should have lower viability under RF exposure. This agrees with many other publications. Taking these discoveries into account, the mechanism of the selectivity of physical cancer treatment can be explained by the resonant behavior of cells under RF exposure. However, the detailed progress of oscillation damaging the membrane and the medium cavitation need be investigated in the future.

Several future improvements and advantages can be expected from plasma-based cancer therapy. First, in CAP, one can control the plasma chemistry, such as specific ion concentrations, to manipulate the frequency resonance to enhance the treatment. So far, many papers have been published to introduce the accurate and automatic control of CAP using machine learning. Second, CAP devices such as plasma jet and dielectric barrier discharge directly have plasma chemistry applied on target to provide RONS. Future works can focus on the resonance coupling and the additional RONS input. Finally, considering the modern RF treatment and plasma therapy, using resonance means optimizing the selectivity that can decrease the total body irradiation, reducing the toxicity.

#### MATERIALS AND METHODS

Glioblastoma cell line U87MG and astrocyte cell line hTERT/E6/E7 were cultured in DMEM (Life Technologies, 11965-118). Melanoma cell line B16F10 was cultured in RPMI-1640 (ATCC 30-2001). All these media were supplemented with 10% (v/v) FBS (GE Healthcare, SH30396) and 1% (v/v) penicillin/streptomycin solution (Life Technologies, 15140122). Cells (2.5  $\times$  10<sup>4</sup> cells/mL) were seeded (3 mL/dish) in a 35 mm cell culture dish (NEST, 706011) and cultured for 24 h under the standard culture condition (a humidified, 37 °C, 5% CO2 environment).

Two types of RF sources are used to apply an electric field to the cells. The first one is a pair of 6 cm  $\times$  6 cm aluminum boards as electrodes set 6 cm away with the Petri dish of cells in the middle. The electric potential applied on the electrodes is sinusoidal 6000 V at 12.5 kHz. This is a single-antenna source, and the cell Petri dish is placed between the electrodes. The dish contains a 100  $\mu$ L cell-culture medium to provide an extracellular environment with a charge

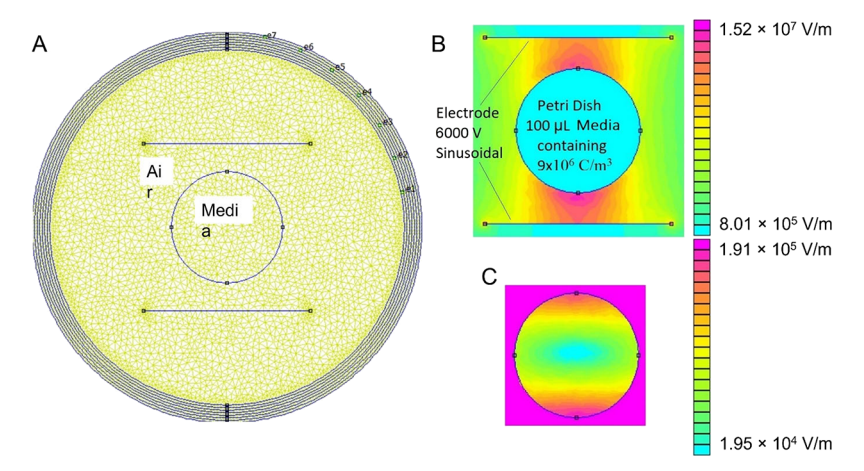
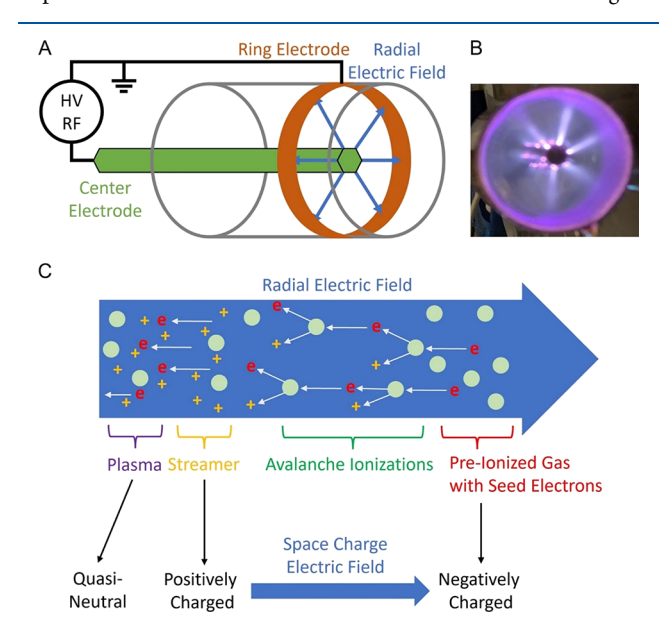


Figure 8. FEMM simulation of the electric field of the plate electrodes. (A) Mesh of such a finite element simulation. (B) Spatially resolved amplitude of the electric field. (C) Lower color scale to show the electric field in media.

density of 10<sup>6</sup> C/m<sup>3</sup> as an average of Na<sup>+</sup>, K<sup>+</sup>, Ca<sub>2</sub><sup>+</sup>, Cl<sup>-</sup>, etc. 19 Therefore, one should expect a sudden change in the refraction index of the electric field at the interface between the media and the air. The electric field cannot be simply estimated by dividing the voltage by the distance between electrodes. To find the amplitude of the electric field, we use FEMM (a finite element electromagnetic simulation software) to compute (Figure 8A). The resulting field amplitude near the Petri dish is found at about  $1.5 \times 10^7 \text{ V/m}$  (Figure 8B). Due to the refraction of the electric field in the cell culture medium (assuming that the electric property is the same as a medical saline solution), the amplitude of the field in the Petri dish is between 1.95  $\times$  10<sup>4</sup> and 1.6  $\times$  10<sup>5</sup> V/m with an average of around 9  $\times$  10<sup>4</sup> V/m (Figure 8C). The second RF source is a plasma generator to provide a multiantenna source as shown in Figure 9. A high-voltage radiofrequency (HVRF) supplies the same 6000 V and 12.5 kHz sinusoidal wave to a pair of electrodes: one is in the center of a helium-filled tube, and the other one is a ring wrapped around the tube (Figure 9A). Radial streamer discharges can thus create cold atmospheric plasma in the tube (Figure 9C), which is commonly used in the field of plasma medicine. 60,61 Note that the center electrode is a hexagonal



**Figure 9.** Radial discharge tube as a cold atmospheric plasma generator. (A) Schematic of the hardware. (B) Front view of the discharge tube, where radial propagations of the streamer can be observed. (C) Physical mechanism of a streamer discharge.

prism that six streamers propagate from the six corners to the outer ring electrode (once per discharge period) as shown in Figure 9B. Therefore, the temporally resolved space charge moves from the center to the circumference. The spatial evolution of the space charge provides an infinity number of 12.5 kHz emission sources. The amplitude of the streamer head potential in the plasma and the potential near the target had been discussed in many previous works. The dish holder is grounded in this work; thus, there is a ground at 5 mm behind the cell, which implies that the electric field is at around 1000 V/m. This is much weaker than the one of the plate electrodes, so we can conclude that the strong effect of the discharge tube is not because of the amplitude but due to the frequency (see the Results and Discussion Section).

To acquire the 3D cell geometry at a microsecond sampling rate synchronized with the external electric field, a Michelson laser interferometer system with a high-speed intensified charge-coupled device (ICCD) camera is used, as shown in Figure 10. The sample (Petri dish with cells in the medium) is placed on the mirror holder, which is a fixed, regular mirror. Before the imaging, the cell media were removed from the Petri dishes, and 30  $\mu$ L of DMEM was added. This can ensure that the effects of cell thickness were significant and exclude the effects of using different media. Next, the laser beam can pass through the cell medium and the transparent Petri dish vertically with no refraction before and after its reflection on the mirror holder (Figure 10A). The fringe image thus shows the disturbance of cells in the area that the 635 nm and 5 mW laser beam can cover. To enlarge the image, the laser passes through a convex lens before the beam splitter, and the mirror sets 1 and 2 reflect the output beam to increase the distance between the ICCD camera and the laser source. The focal length of the convex lens is 6 mm, and the distance is 4.7 m. This gives a zoom-in about 786 times, and a cell with a 10  $\mu$ m diameter can be enlarged to 7.9 mm on a screen at the location of the ICCD camera.

Based on the natural frequency of the cell model, <sup>17</sup> which will also be derived in the next chapter, we expect the cells to be able to react to the external electric field at radiofrequencies. Therefore, assuming the cell deformation is repeated identically in each period (in this experiment, the value is 80  $\mu$ s for the 12.5 kHz), the exposure window width of the ICCD camera is 2  $\mu$ s where each window in each period is triggered after a unique delay time. The delay time is linearly increased from 0  $\mu$ s with a step of 2  $\mu$ s to the final 800  $\mu$ s after a 400-image recording. Therefore, multiple-period observation can be used to confirm a repeating cell behavior at the same frequency as the external electric field.

AFM measurements were done at an ambient temperature in the fluidic cell culture media with an MFP-3D (Asylum Research) microscope using a CP-CONT-BSG-C 20  $\mu$ m colloidal probe. The cantilever spring constant was found to be 0.291 N/m by thermal calibration using Sader's method provided by the Asylum Research

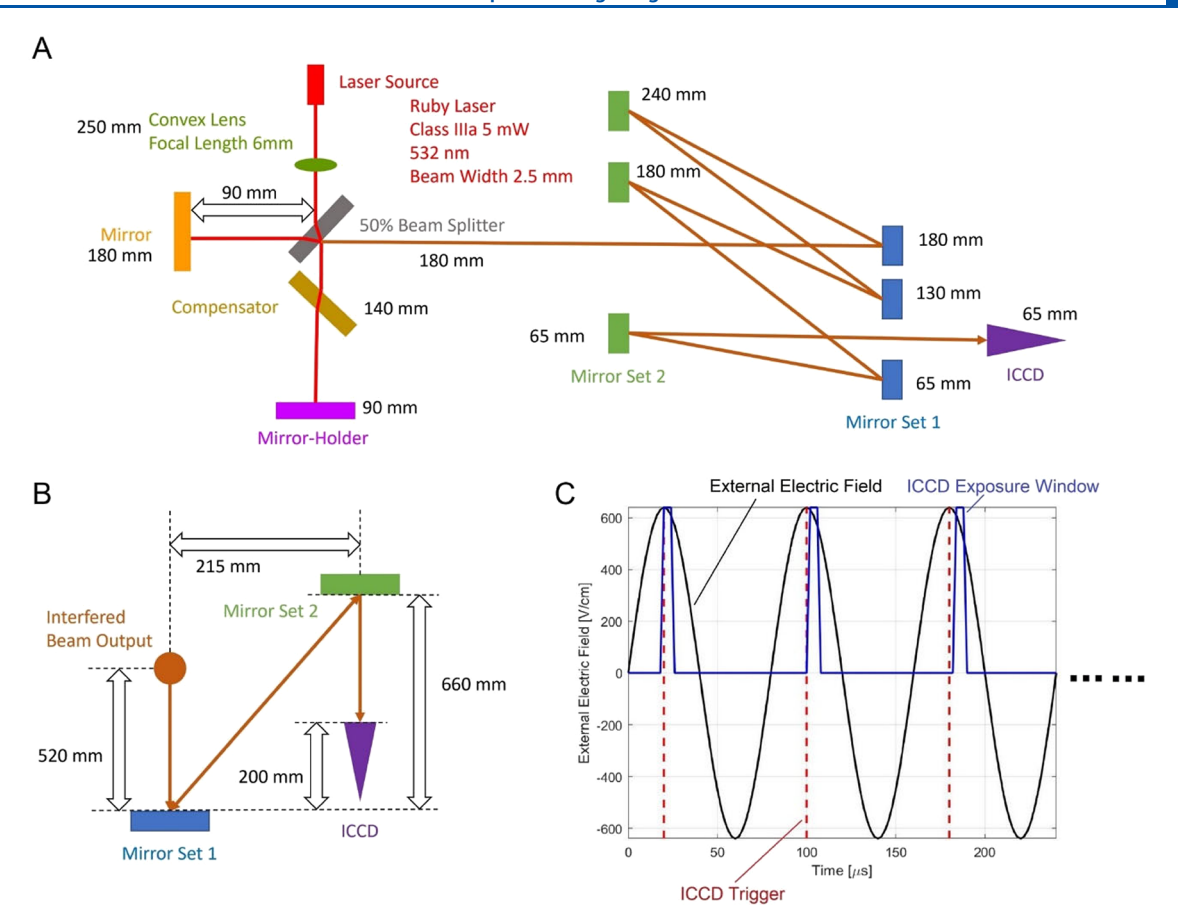


Figure 10. Experimental setups of the laser Michelson interferometer. (A) Side view of the hardware setup showing the Michelson laser interferometer with optical components and the high-speed ICCD camera. (B) Top view. (C) Temporal setup of the ICCD camera is synchronized with the external electric field, and each window is triggered after a linearly increasing delay to capture the periodic cell geometry.

software.<sup>63</sup> Six cell lines of force spectroscopy experiments were performed in which the central regions of 5 different cells were probed 10 times. Each set of experiments took no more than 10 min to minimize any environmental effects that may occur within the cells. In total, 100 quasistatic force curves were collected for each cell type. Each force curve was specified for a 500 nm/s approach velocity, 50 kHz sampling frequency, and 3.7 nN maximum set force to avoid violating the small deformation criteria of the contact mechanics formulation.<sup>64</sup>

The relaxance spectra for each cell type were calculated per the Lee and Radok contact mechanics formulation.  $^{37,38,64}$  As seen in eq 7, after transforming each set of force curves into the Z-domain, they are averaged among themselves, and the relaxance spectra can be calculated. Then, an SLS model (given as eq 8) is fit to the relaxance spectra for each cell line to obtain the glassy modulus, equilibrium modulus, and viscosity of the cells.

$$Q(z) = \frac{\sigma(z)}{\varepsilon(z)} = \frac{3}{16\sqrt{R}} \frac{\sum_{i=0}^{N} Z[f_i(t)]}{\sum_{i=0}^{N} Z[h_i(t)]^{3/2}}$$
(7)

$$Q(z) = G_{g} - \frac{G}{1 + \frac{\mu}{G\Delta t}(1 - z^{-1})}$$
(8)

The relaxance can be used to calculate the response of each cell from either a stress or strain input. As demonstrated in the main paper, the strain response due to a harmonic stress, like a cell's resonance frequency  $f_{\eta \nu}$  can be obtained by multiplying the relaxance (the mechanical transfer function of the cell) with the form of the harmonic stress in the Z-domain. For example, in the calculations from Figure 3B, the relaxance was taken as the fitted values from eq 8

to minimize the effects of noise in the neighborhood around the natural frequency in the stress input.

For physical factor CAP treatment before confocal imaging, media were removed, the Petri dish was inverted with the lid on, and the cells were treated for 60 s at a distance of 2 cm from the CAP source. The media were then replaced, and the cells were cultured for 10 min in the cell culture incubator (37 °C, 5% CO<sub>2</sub>). After 10 min, the media was removed and 4% paraformaldehyde fixative was added to halt cellular changes for more accurate timing during imaging and to remove any phototoxic effects of laser light during imaging. The cells were fixed for 30 min with the three dyes denoted: Hoechst 33342 (nuclear stain - blue) (Thermo Fisher, Waltham, MA), Biotracker 488 (microtubules – green) (Sigma-Aldrich, St. Louis, MO), and Cell Mask deep red (plasma membrane - red) (Thermo Fisher, Waltham, MA). The cells were then imaged on the Zeiss spinning disk confocal microscope in the GW imaging and nanofabrication facility in Z stacks. The images displayed are of a single plane of the Z stack. Laser intensity and exposure times were maintained throughout the experiment for comparison between samples.

The cell sensitization experiment was designed as follows: The research strategy was based on 10 different experimental groups. The 1st experimental group is the control group. The cell culture media were removed from the cell culture dish. After 7 min, 3 mL of fresh cell culture media was added to the cells. The 2nd experimental group is the TMZ-only group. The cell culture media was removed from the cell culture dish. After a 7 min waiting, 3 mL of fresh cell culture media with 500  $\mu$ M TMZ was added to the cells. The 3rd experimental group is the "discharge tube only" group. The cell culture media were removed before the treatment. After that, the cells were treated by placing the cell culture dish on the discharge tube at a distance of 1 mm for 7 min. After the treatment, 3 mL of fresh cell culture media was added to the cells. The 4th group is the "discharge

tube + TMZ" group. The cells were treated with the discharge tube for 7 min without media. After that, 3 mL of fresh cell culture media with 500  $\mu M$  TMZ was added to the cells. The 5th group is the "electrodes only" group. The cell culture media was removed, and then the cell culture dish was placed between the electrodes for 7 min. After that, 3 mL of fresh cell culture media was added to the cells after the treatment. The 6th group is the "electrodes + TMZ" group. This is a similar protocol to the 4th group, but the plasma treatment is replaced with the electrodes. The 7th group is the "microwave only" group. The cell culture media was removed, and then the cell culture dish was placed in front of a WR75 microwave horn antenna for 7min. The microwave horn antenna emits a 5 mW 8-18 GHz frequency-sweep microwave generated from an HP 8350B sweep oscillator with an HP 86251A RF Plug-in option. The frequencysweep period is 0.1 s. After that, 3 mL of fresh cell culture media was added to the cells after the treatment. The 8th group is the "microwave + TMZ" group. This is also a similar protocol to the 4th group, but the plasma treatment is replaced with microwave radiation. The 9th group is the "electrodes + microwave" group. The cell culture media were also removed before the treatment for this group. Then, the cells were treated with the 12.5 kHz electric field from the electrodes and the frequency-sweep microwave together for 7 min. The 12.5 kHz field is parallel to the H plane of the microwave horn. After that, 3 mL of fresh cell culture media was added to the cells after the treatment. The last group is the "electrodes + microwave + TMZ" group. This is a similar group to the 9th one, but after the electrode and microwave treatment, 3 mL of cell culture media with 500 µM TMZ was added to the cells after the treatment.

#### AUTHOR INFORMATION

#### **Corresponding Authors**

Li Lin — Micropropulsion and Nanotechnology Laboratory, School of Engineering and Applied Science, George Washington University, Washington, D.C. 20052, United States of America; orcid.org/0000-0003-0176-8858; Email: lilin@gwu.edu

Michael Keidar — Micropropulsion and Nanotechnology Laboratory, School of Engineering and Applied Science, George Washington University, Washington, D.C. 20052, United States of America; Email: keidar@gwu.edu

#### **Authors**

Marshall R. McCraw — Scanning Probe Microscopy Laboratory, School of Engineering and Applied Science, George Washington University, Washington, D.C. 20052, United States of America

Berkin Uluutku — Scanning Probe Microscopy Laboratory, School of Engineering and Applied Science, George Washington University, Washington, D.C. 20052, United States of America

Yi Liu – School of Mechanical Engineering, Shanghai Jiaotong University, Shanghai 200240, People's Republic of China

Dayun Yan — Micropropulsion and Nanotechnology Laboratory, School of Engineering and Applied Science, George Washington University, Washington, D.C. 20052, United States of America; ◎ orcid.org/0000-0002-9801-021X

Vikas Soni – Micropropulsion and Nanotechnology Laboratory, School of Engineering and Applied Science, George Washington University, Washington, D.C. 20052, United States of America

Alex Horkowitz – Micropropulsion and Nanotechnology Laboratory, School of Engineering and Applied Science, George Washington University, Washington, D.C. 20052, United States of America Xiaoliang Yao — Micropropulsion and Nanotechnology Laboratory, School of Engineering and Applied Science, George Washington University, Washington, D.C. 20052, United States of America

Ruby Limanowski — Micropropulsion and Nanotechnology Laboratory, School of Engineering and Applied Science, George Washington University, Washington, D.C. 20052, United States of America

Santiago D. Solares — Scanning Probe Microscopy Laboratory, School of Engineering and Applied Science, George Washington University, Washington, D.C. 20052, United States of America

Isak I. Beilis — School of Electrical Engineering, Tel Aviv University, 6997801 Tel Aviv-Yafo, Israel

Complete contact information is available at: https://pubs.acs.org/10.1021/acs.langmuir.2c03181

#### **Author Contributions**

 $^{\P}$ M.R.M., B.U., and Y.L. contributed equally. L.L., M.K., and I.I.B. contributed to the main concept of this work. L.L. established the laser Michaelson interferometry system and completed the measurement of cell membrane oscillations. L.L. and Y.L. contributed to the POD analysis of the cell images recorded by the ICCD camera. L.L. computed the effective charge densities, resonant frequencies, and effective current densities and contributed to all further data analysis. A.H., M.R.M., B.U., V.S., and S.D.S. contributed to the AFM measurement of cell membrane stiffness. A.H. contributed to the confocal cell imaging. X.Y. and D.Y. cultured the B16F10, hTERT/E6/E7, and U87MG cells while X.Y. made the U87MG sensitization test. X.Y. also cultured the L929 cells. V.S. cultured the A549 and BEAS-2B cells. L.L. contributed to the initial manuscript. All authors contributed to the manuscript editing.

#### **Funding**

This research was funded by Charlie Teo Foundation and a National Science Foundation grant, grant number 1747760.

#### Notes

The authors declare no competing financial interest.

#### REFERENCES

- (1) Chu, K. F.; Dupuy, D. E. Thermal ablation of tumours: Biological mechanisms and advances in therapy. *Nat. Rev. Cancer* **2014**. *14*. 199.
- (2) Gorin, M. A.; Allaf, M. E. Kidney cancer: Radiofrequency ablation of small renal masses More work required. *Nat. Rev. Urol.* **2012**, *9*, 297.
- (3) Isambert, H. Understanding the electroporation of cells and artificial bilayer membranes. *Phys. Rev. Lett.* **1998**, *80*, 3404.
- (4) Devyatkov, N. D.; Golant, M. B.; Betskiy, O. V. Millimeter waves and their role in the processes of life activities. *Moscow, Radio Commun.* **1991**, 168.
- (5) Szabo, I.; Kappelmayer, J.; Alekseev, S. I.; Ziskin, M. C. Millimeter wave induced reversible externalization of phosphatidylserine molecules in cells exposed in vitro. *Bioelectromagnetics* **2006**, 27, 233.
- (6) Sentsov, A. A.; Bukaeva, I. G.; Neuimina, G. I. Features of using extremely high-frequency low-intensity electromagnetic radiation in medical practice. 2021 Wave Electronics and Its Application in Information and Telecommunication Systems (WECONF); 2021, 1–5.
- (7) Anton, E.; Rotaru, A.; Covatariu, D.; Ciobica, A.; Timofte, D.; Popescu, R.; Anton, C. Links between extremely high frequency electromagnetic waves and their biological manifestations. *Arch. Biol. Sci.* **2015**, *67*, 895.

- (8) Fedorov, V. I.; Popova, S. S.; Pisarchik, A. N. Dynamic effects of submillimeter wave radiation on biological objects of various levels of organization. *Int. J. Infrared Millimeter Waves* **2003**, *24*, 1235.
- (9) Logani, M. K.; Szabo, I.; Makar, V.; Bhanushali, A.; Alekseev, S.; Ziskin, M. C. Effect of millimeter wave irradiation on tumor metastasis. *Bioelectromagnetics* **2006**, *27*, 258.
- (10) Yan, D.; Xu, W.; Yao, X.; Lin, L.; Sherman, J. H.; Keidar, M. The cell activation phenomena in the cold atmospheric plasma cancer treatment. *Sci. Rep.* **2018**, *8*, 15418.
- (11) Riske, K. A.; Dimova, R. Electro-deformation and poration of giant vesicles viewed with high temporal resolution. *Biophys. J.* **2005**, 88, 1143.
- (12) Astumian, R. D.; Robertson, B. Nonlinear effect of an oscillating electric field on membrane proteins. *J. Chem. Phys.* **1989**, *91*, 4891.
- (13) Taghian, T.; Narmoneva, D. A.; Kogan, A. B. Modulation of cell function by electric field: a high-resolution analysis. *J. R. Soc., Interface* **2015**, *12*, 20150153.
- (14) Escoffre, J.-M.; Dean, D. S.; Hubert, M.; Rols, M.-P.; Favard, C. Membrane perturbation by an external electric field: A mechanism to permit molecular uptake. *Eur. Biophys. J.* **2007**, *36*, 973.
- (15) Fröhlich, H. Bose condensation of strongly excited longitudinal electric modes. *Phys. Lett. A* **1968**, 26, 402.
- (16) Fröhlich, H. Long-range coherence and energy storage in biological systems. *Int. J. Quantum Chem.* **1968**, *2*, 641.
- (17) Martinez, L.; Dhruv, A.; Lin, L.; Balaras, E.; Keidar, M. Model for deformation of cells from external electric fields at or near resonant frequencies. *Biomed. Phys. Eng. Express* **2020**, *6*, No. 065022.
- (18) Kontorovich, V. M.; Glutsyuk, A. M. Transformation of sound and electromagnetic waves at the boundary of a conductor in a magnetic field. *Sov. Phys. JETP* **1962**, *14*, 852.
- (19) Shneider, M. N.; Pekker, M. Stimulated activity in the neural tissue. J. Appl. Phys. 2019, 125, 211101.
- (20) Ma, Y.; Poole, K.; Goyette, J.; Gaus, K. Introducing membrane charge and membrane potential to T cell signaling. *Front. Immunol.* **2017**, *8*, 1513.
- (21) Yang, M.; Brackenbury, W. J. Membrane potential and cancer progression. *Front. Physiol.* **2013**, *4*, 185.
- (22) Keidar, M. *Plasma Cancer Therapy*; Springer: Berlin, Germany, 2020.
- (23) von Woedtke, T.; Laroussi, M.; Gherardi, M. Foundations of plasmas for medical applications. *Plasma Sources Sci. Technol.* **2022**, 31, No. 054002.
- (24) Laroussi, M.; Bekeschus, S.; Keidar, M.; Bogaerts, A.; Fridman, A.; Lu, X.; Ostrikov, K.; Hori, M.; Stapelmann, K.; Miller, V.; Reuter, S.; Laux, C.; Mesbah, A.; Walsh, J.; Jiang, C.; Thagard, S. M.; Tanaka, H.; Liu, D.; Yan, D.; Yusupov, M. Low-temperature plasma for biology, hygiene, and medicine: Perspective and roadmap. *IEEE Trans. Radiat. Plasma Med. Sci.* 2022, 6, 127.
- (25) Yan, D.; Wang, Q.; Adhikari, M.; Malyavko, A.; Lin, L.; Zolotukhin, D. B.; Yao, X.; Kirschner, M.; Sherman, J. H.; Keidar, M. A physically triggered cell death via transbarrier cold atmospheric plasma cancer treatment. ACS Appl. Mater. Interfaces 2020, 12, 34548.
- (26) Yao, X.; Lin, L.; Soni, V.; Gjika, E.; Sherman, J. H.; Yan, D.; Keidar, M. Sensitization of glioblastoma cells to temozolomide by a helium gas discharge tube. *Phys. Plasmas* **2020**, *27*, 114502.
- (27) Lin, L.; Lyu, Y.; Trink, B.; Canady, J.; Keidar, M. Cold atmospheric helium plasma jet in humid air environment. *J. Appl. Phys.* **2019**, *125*, 153301.
- (28) Yao, X.; Yan, D.; Lin, L.; Sherman, J. H.; Peters, K. B.; Keir, S. T.; Keidar, M. Cold plasma discharge tube enhances antitumoral efficacy of temozolomide. *ACS Appl. Biomater.* **2022**, *5*, 1610.
- (29) Lin, L.; Keidar, M. A map of control for cold atmospheric plasma jets: From physical mechanisms to optimizations. *Appl. Phys. Rev.* **2021**. 8. No. 011306.
- (30) Liang, Y. C.; Lee, H. P.; Lim, S. P.; Lin, W. Z.; Lee, K. H.; Wu, C. G. Proper orthogonal decomposition and its applications Part I: Theory. *J. Sound Vib.* **2002**, *252*, 527.

- (31) Berkooz, G.; Holmes, P.; Lumley, J. L. The proper orthogonal decomposition in the analysis of turbulent flows. *Annu. Rev. Fluid Mech.* **1993**, 25, 539.
- (32) Kang, S. W.; Atluri, S. N. Free vibration analysis of arbitrarily shaped polygonal plates with simply supported edges using a subdomain method. *J. Sound Vib.* **2009**, 327, 271.
- (33) Robertson, S. R. Solving the problem of forced motion of viscoelastic plates by valanis' method with an application to a circular plate. *J. Sound Vib.* **1971**, *14*, 263.
- (34) Johnson, S. M.; Buttress, N. The osmotic insensitivity of sonicated liposomes and the density of phospholipid-cholesterol mixtures. *Biochim. Biophys. Acta* 1973, 307, 20.
- (35) Terzi, M. M.; Deserno, M.; Nagle, J. F. Mechanical properties of lipid bilayers: A note on the Poisson ratio. *Soft Matter* **2019**, *15*, 9085.
- (36) Jadidi, T.; Seyyed-Allaei, H.; Tabar, M. R. R.; Mashaghi, A. Poisson's ratio and Young's modulus of lipid bilayers in different phases. *Front. Bioeng. Biotechnol.* **2014**, *2*, 8.
- (37) Uluutku, B.; López-Guerra, E. A.; Solares, S. D. A new method for obtaining model-free viscoelastic material properties from atomic force microscopy experiments using discrete integral transform techniques. *Beilstein J. Nanotechnol.* **2021**, *12*, 1063.
- (38) Uluutku, B.; McCraw, M. R.; Solares, S. D. Direct measurement of storage and loss behavior in AFM force-distance experiments using the modified Fourier transformation. *J. Appl. Phys.* **2022**, *131*, 165101.
- (39) Wang, K.; Zhao, Y.; Chen, D.; Fan, B.; Lu, Y.; Chen, L.; Long, R.; Wang, J.; Chen, J. Specific membrane capacitance, cytoplasm conductivity and instantaneous Young's modulus of single tumour cells. *Sci. Data* **2017**, *4*, 170015.
- (40) Lulevich, V.; Zink, T.; Chen, H. Y.; Liu, F. T.; Liu, G. Y. Cell mechanics using atomic force microscopy-based single-cell compression. *Langmuir* **2006**, *22*, 8151.
- (41) Souza, S. T.; Agra, L. C.; Santos, C. E. A.; Barreto, E.; Hickmann, J. M.; Fonseca, E. J. S. Macrophage adhesion on fibronectin evokes an increase in the elastic property of the cell membrane and cytoskeleton: An atomic force microscopy study. *Eur. Biophys. J.* **2014**, *43*, 573.
- (42) Suresh, S. Biomechanics and biophysics of cancer cells. *Acta Mater.* **2007**, *55*, 3989.
- (43) Yan, D.; Horkowitz, A.; Wang, Q.; Keidar, M. On the selective killing of cold atmospheric plasma cancer treatment: Status and beyond. *Plasma Processes Polym.* **2021**, *18*, 2100020.
- (44) Yan, D.; Wang, Q.; Malyavko, A.; Zolotukhin, D. B.; Adhikari, M.; Sherman, J. H.; Keidar, M. The anti-glioblastoma effect of cold atmospheric plasma treatment: physical pathway v.s. chemical pathway. Sci. Rep. 2020, 10, 11788.
- (45) Ja Kim, S.; Min Joh, H.; Chung, T. H. Production of intracellular reactive oxygen species and change of cell viability induced by atmospheric pressure plasma in normal and cancer cells. *Appl. Phys. Lett.* **2013**, *103*, 153705.
- (46) Yan, D.; Lin, L.; Sherman, J. H.; Canady, J.; Trink, B.; Keidar, M. The correlation between the cytotoxicity of cold atmospheric plasma and the extracellular H<sub>2</sub>O<sub>2</sub> scavenging rate. *IEEE Trans. Radiat. Plasma Med. Sci.* **2018**, *2*, 618.
- (47) Passechnik, V. I.; Hianik, T.; Karagodin, V. P.; Kagan, V. E. Elasticity, strength and stability of bilayer lipid membranes and their changes due to phospholipid modification. *Gen. Physiol. Biophys.* **1984**, *3*, 475.
- (48) Wood, A. K. W.; Sehgal, C. M. A review of low-intensity ultrasound for cancer therapy. *Ultrasound Med. Biol.* 2015, 41, 905.
- (49) Rosenthal, I.; Sostaric, J. Z.; Riesz, P. Sonodynamic therapy—a review of the synergistic effects of drugs and ultrasound. *Ultrason. Sonochem.* **2004**, *11*, 349.
- (50) Trendowski, M. The promise of sonodynamic therapy. *Cancer Metastasis Rev.* **2014**, 33, 143.
- (51) Costley, D.; Mc Ewan, C.; Fowley, C.; McHale, A. P.; Atchison, J.; Nomikou, N.; Callan, J. F. Treating cancer with sonodynamic therapy: A review. *Int. J. Hyperthermia* **2015**, *31*, 107.

- (52) Yan, D.; Malyavko, A.; Wang, Q.; Lin, L.; Sherman, J. H.; Keidar, M. Cold atmospheric plasma cancer treatment, a critical review. *Appl. Sci.* **2021**, *11*, 7757.
- (53) Graves, D. B. Reactive species from cold atmospheric plasma: Implications for cancer therapy. *Plasma Processes Polym.* **2014**, *11*, 1120.
- (54) Wang, X.; Zhong, X.; Gong, F.; Chao, Y.; Cheng, L. Newly developed strategies for improving sonodynamic therapy. *Mater. Horiz.* **2020**, 7, 2028.
- (55) Choi, E. H.; Uhm, H. S.; Kaushik, N. K. Plasma bioscience and its application to medicine. *AAPPS Bull.* **2021**, *31*, 10.
- (56) Calò, A.; Reguera, D.; Oncins, G.; Persuy, M.-A.; Sanz, G.; Lobasso, S.; Corcelli, A.; Pajot-Augy, E.; Gomila, G. Force measurements on natural membrane nanovesicles reveal a composition-independent, high Young's modulus. *Nanoscale* **2014**, *6*, 2275.
- (57) Lin, L.; Yan, D.; Lee, T.; Keidar, M. Self-adaptive plasma chemistry and intelligent plasma medicine. *Adv. Intell. Syst.* **2022**, *4*, 2100112.
- (58) Bonzanini, A. D.; Graves, D. B.; Mesbah, A. Learning-based SMPC for reference tracking under state-dependent uncertainty: An application to atmospheric pressure plasma jets for plasma medicine. *IEEE Trans. Control Syst. Technol.* **2022**, *30*, 611.
- (59) Wang, Q.; Malyavko, A.; Yan, D.; Lamanna, O. K.; Hsieh, M. H.; Sherman, J. H.; Keidar, M. A comparative study of cold atmospheric plasma treatment, chemical versus physical strategy. *J. Phys. D: Appl. Phys.* **2021**, *54*, No. 095207.
- (60) Park, S.; Choe, W.; Lee, H.; Park, J. Y.; Kim, J.; Moon, S. Y.; Cvelbar, U. Stabilization of liquid instabilities with ionized gas jets. *Nature* **2021**, *592*, 49.
- (61) Lu, X.; Ostrikov, K. Guided ionization waves: The physics of repeatability. *Appl. Phys. Rev.* **2018**, *5*, No. 031102.
- (62) Soni, V.; Adhikari, M.; Simonyan, H.; Lin, L.; Sherman, J. H.; Young, C. N.; Keidar, M. In vitro and in vivo enhancement of temozolomide effect in human glioblastoma by non-invasive application of cold atmospheric plasma. *Cancers* **2021**, *13*, 4485.
- (63) Sader, J. E.; Chon, J. W. M.; Mulvaney, P. Calibration of rectangular atomic force microscope cantilevers. *Rev. Sci. Instrum.* 1999, 70, 3967.
- (64) Lee, E. H.; Radok, J. R. M. The contact problem for viscoelastic bodies. *J. Appl. Mech.* **1960**, *27*, 438.

### **□** Recommended by ACS

## Proteomes of Micro- and Nanosized Carriers Engineered from Red Blood Cells

Chi-Hua Lee, Bahman Anvari, et al.

FEBRUARY 15, 2023

JOURNAL OF PROTEOME RESEARCH

READ 🗹

# **Evaluating Subtle Pathological Changes in Early Myocardial Ischemia Using Spectral Histopathology**

Tian Tian, Yijiu Chen, et al.

NOVEMBER 28, 2022

ANALYTICAL CHEMISTRY

READ 🗹

## THz-PCR Based on Resonant Coupling between Middle Infrared and DNA Carbonyl Vibrations

Na Li and Feng Zhang

FEBRUARY 01, 2023

ACS APPLIED MATERIALS & INTERFACES

READ 🗹

#### CRISPR Cas12a-Powered Silicon Surface-Enhanced Raman Spectroscopy Ratiometric Chip for Sensitive and Reliable Quantification

Haiting Cao, Houyu Wang, et al.

JANUARY 19, 2023

ANALYTICAL CHEMISTRY

READ 🗹

Get More Suggestions >